

Stretchable, Breathable, and Stable Lead-Free Perovskite/Polymer Nanofiber Composite for Hybrid Triboelectric and Piezoelectric Energy Harvesting

Feng Jiang, Xinran Zhou, Jian Lv, Jian Chen, Juntong Chen, Haruethai Kongcharoen, Yihui Zhang, and Pooi See Lee*

Halide-perovskite-based mechanical energy harvesters display excellent electrical output due to their unique ferroelectricity and dielectricity. However, their high toxicity and moisture sensitivity impede their practical applications. Herein, a stretchable, breathable, and stable nanofiber composite (LPPS-NFC) is fabricated through electrospinning of lead-free perovskite/poly(vinylidene fluoride-co-hexafluoropropylene) (PVDF-HFP) and styrene-ethylene-butylene-styrene (SEBS). The $\text{Cs}_3\text{Bi}_2\text{Br}_9$ perovskites serve as efficient electron acceptors and local nucleating agents for the crystallization of polymer chains, thereby enhancing the electron-trapping capacity and polar crystalline phase in LPPS-NFC. The excellent energy level matching between $\text{Cs}_3\text{Bi}_2\text{Br}_9$ and PVDF-HFP boosts the electron transfer efficiency and reduces the charge loss, thereby promoting the electron-trapping process. Consequently, this LPPS-NFC-based energy harvester displays an excellent electrical output (400 V, 1.63 $\mu\text{A cm}^{-2}$, and 2.34 W m^{-2}), setting a record of the output voltage among halide-perovskite-based nanogenerators. The LPPS-NFC also exhibits excellent stretchability, waterproofness, and breathability, enabling the fabrication of robust wearable devices that convert mechanical energy from different biomechanical motions into electrical power to drive common electronic devices. The LPPS-NFC-based energy harvesters also endure extreme mechanical deformations (washing, folding, and crumpling) without performance degradation, and maintain stable electrical output up to 5 months, demonstrating their promising potential for use as smart textiles and wearable power sources.

1. Introduction

Wearable electronics, an emerging technology that achieves the flexibility, wearability, and comfortability of our daily electronic devices, can be widely employed in various applications, such as electronic skin,^[1–4] self-powered sensors,^[5] and health monitoring.^[6,7] Although great progress has been dedicated to developing multifunctional wearable devices, the power supply is still an intractable challenge to be tackled. Batteries and supercapacitors, despite the good stability and efficiency, are still limited in their restricted lifetime, rigidity, bulkiness, encapsulation, and safety issues.^[8,9] As prospective candidates for the future self-powered techniques, triboelectric and piezoelectric nanogenerators (TEGs and PENGs) enable the harvesting of mechanical energy from both environment (wind, rain, and tidal energy) and human motions (walking, running, clapping, and elbow bending), and convert them into the electricity to power wearable devices.^[10–15] TEGs generate electricity via a coupled effect of triboelectrification and electrostatic induction, while PENGs transform mechanical energy to electricity by utilizing the dipole moment through the deformation of piezoelectric materials.

Both of them are promising energy techniques that can satisfy demanding requirements of the green energy as well as the sustainable development. However, these two techniques also have different advantages and drawbacks. For example, PENGs usually own better electrical stability and operational flexibility in view of the convenient encapsulation to the piezoelectric materials and inherent structure dexterity, but their electrical output is relatively low. In contrast, TEGs typically have higher electrical output, but their working mechanisms, such as vertical contact-separation and lateral sliding modes, require the relative displacement of two different materials, which restrict the configuration of the device and application scenarios. Therefore, a hybrid TENG and PENG energy harvester (TPENG), combining their advantages, is highly desirable to acquire higher power output and adapt to different applications.

F. Jiang, X. Zhou, J. Lv, J. Chen, J. Chen, H. Kongcharoen, P. S. Lee
School of Materials Science and Engineering
Nanyang Technological University
50 Nanyang Avenue, Singapore 639798, Singapore
E-mail: pslee@ntu.edu.sg

F. Jiang
Institute of Flexible Electronics Technology of Tsinghua
Zhejiang, Jiaying 314000, China

Y. Zhang
Applied Mechanics Laboratory
Department of Engineering Mechanics
Center for Flexible Electronics Technology
Tsinghua University
Beijing 100084, China

 The ORCID identification number(s) for the author(s) of this article can be found under <https://doi.org/10.1002/adma.202200042>.

DOI: 10.1002/adma.202200042

Tremendous efforts have been made to explore the potential materials and structures to develop TPENGs with high electrical output.^[16–20] Among various materials, poly(vinylidene fluoride) (PVDF) and its copolymers are popular candidates considering their outstanding triboelectric and piezoelectric performance.^[21–23] For instance, poly(vinylidene fluoride-co-hexafluoropropylene) (PVDF-HFP) exhibits great electronegativity due to the high fluorine content, which can serve as competitive triboelectric negative layers for TENG.^[24,25] Meanwhile, PVDF-HFP is also a powerful piezoelectric material owing to its ferroelectric β phase.^[26–29] Nonetheless, with the increasing number of electronic devices and denser device integration, typical PVDF-HFP-based nanogenerators are not enough to meet the escalating requirements of energy consumption. A promising way that can increase the electrical output of PVDF-HFP is to modify the physical and chemical properties of PVDF-HFP by adding functional fillers. Among different additives, halide perovskite, a promising material in the field of solar cells,^[30] photodetector,^[31] and light-emitting diode (LED),^[32] displays huge potential as promotive additives to enhance both TENG and PENG performance.^[33,34] Compared to other materials, e.g., zinc oxide (ZnO),^[35] reduced graphene oxide (rGO),^[36] and molybdenum disulfide (MoS₂),^[37] halide perovskites could exhibit unique advantages in the mechanical energy harvesting that follows from their flexible energy level tunability. The energy levels of halide perovskites are easily regulated by composition optimization, allowing the energy level alignment between the perovskite and PVDF-HFP, which can minimize the charge loss and enhance the charge transfer efficiency, thereby promoting the electrical output.^[38–40] In addition, perovskites also have many intrinsic defects, which can serve as efficient charge acceptors to store and attract more charges, contributing to the triboelectric output.^[41,42] Moreover, the semi-conducting and ionic properties of perovskites enable them to serve as effective nucleating agents that facilitate the conversion of amorphous or nonpolar phase into polar β -crystalline phase for PVDF-HFP, favoring better piezoelectric performance.^[43–45] Hence, halide perovskites are ideal additives to improve both triboelectric and piezoelectric output.

In spite of these inspiring advantages, existing studies still mostly focused on the lead-based halide perovskites,^[46–48] which may cause damage to both human health and environment due to the toxic lead elements. Some other lead-free perovskites, for instance, the tin-based perovskites, despite low toxicity, suffer from the instability and oxidation issues.^[34,49] Compared to these perovskites, bismuth-based perovskites are more desirable considering their low toxicity and good stability.^[50,51] Another challenge for the practical application of halide perovskites is their brittle nature, which could easily result in the material failure during mechanical deformations of wearable devices. Integrating the perovskites into flexible PVDF-HFP to form a uniform composite endows exceptional mechanical durability and flexibility to the perovskites, and the PVDF-HFP also offers an extra protective layer to avoid the direct contact between perovskites and the external atmosphere; thus the mechanical property and stability can be significantly improved.

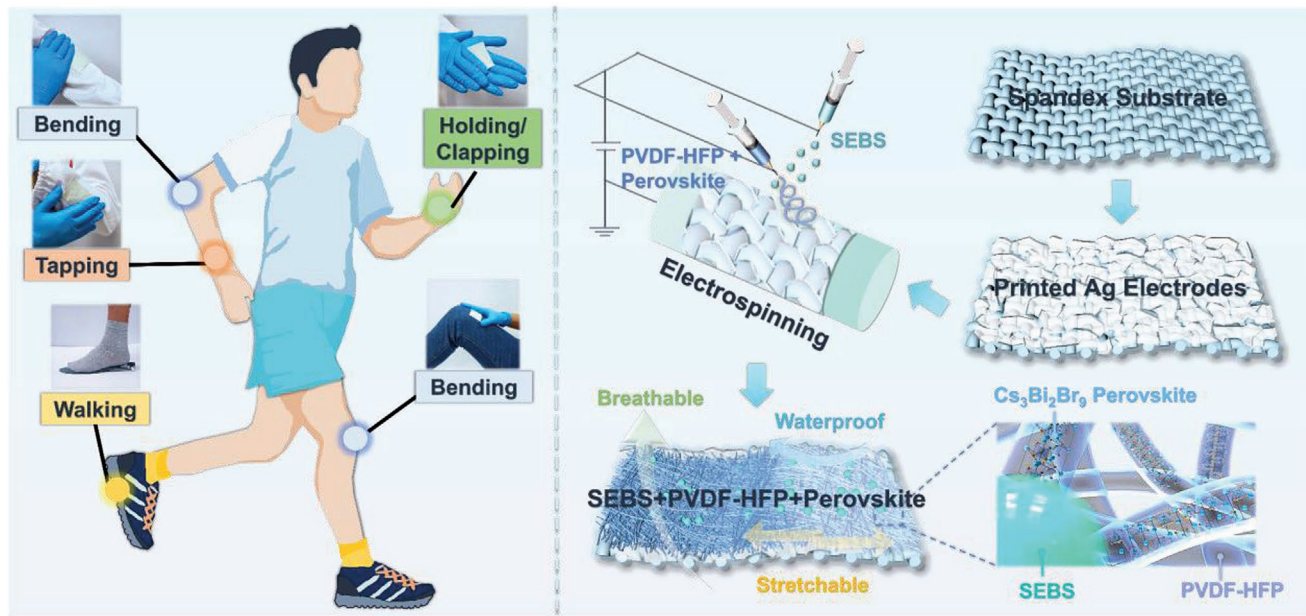
Herein, we adopt Cs₃Bi₂Br₉ to design a stretchable, breathable, and stable nanofiber composite (LPPS-NFC) using electrospinning of lead-free perovskite/PVDF-HFP and

styrene–ethylene–butylene–styrene (SEBS). The incorporation of Cs₃Bi₂Br₉ into the PVDF-HFP nanofibers can serve as efficient electron acceptors and local nucleating agents, which improve the electron-trapping ability and polar crystalline phase of LPPS-NFC. Besides, the excellent energy level matching between Cs₃Bi₂Br₉ and PVDF-HFP also promotes the electron transfer efficiency and reduces the charge loss, further enhancing the electrical performance. By virtue of these unique advantages of Cs₃Bi₂Br₉, the LPPS-NFC displays substantially enhanced output voltage and current density of 400 V and 1.63 $\mu\text{A cm}^{-2}$ (peak-to-peak values), where the output voltage is the highest among reported halide-perovskite-based mechanical energy harvesters. Moreover, the stability and charge retention capacity of perovskites have been largely strengthened due to the encapsulation and protection of PVDF-HFP. The addition of SEBS can also function as hydrophobic modifiers and elastic binders, bestowing excellent waterproofness and stretchability to the LPPS-NFC. Furthermore, the well-designed LPPS-NFC energy harvesters also possess excellent electrostatic adhesion, breathability, deformation resistance, durability, and stability, which can maintain excellent electrical performance after extreme mechanical deformations (washing, folding, and crumpling) and sustain stable electrical output up to 5 months, suggesting their great potential as self-powered materials for wearable devices.

2. Results and Discussion

Scheme 1 displays the fabrication process of stretchable, breathable, and stable LPPS-NFC-based energy harvester and its potential applications in wearable power sources for collecting electricity from human motions. Spandex is selected as substrate in light of its good breathability and stretchability. Then the silver–SEBS ink is printed on the spandex as stretchable conductors through screen printing, where the silver and SEBS function as conductive fillers and stretchable binders, respectively. Subsequently, the whole conductive textile is mounted on the metallic collector for electrospinning (ES), allowing the LPPS-NFC to bind on the printed stretchable electrodes. During the ES process, one syringe is loaded with a mixed solution of PVDF-HFP and Cs₃Bi₂Br₉, while the other one is filled with SEBS solution. Under the high electrical field and fast-rolling speed, the mixed solution will form a uniform composite and perovskites are embedded into PVDF-HFP nanofibers. In the meantime, the SEBS microspheres, serving as elastic binders, are injected into the nanofiber composite, which mechanically interlock the nanofibers and endow the whole nanofiber composite with excellent stretchability and waterproofness. Finally, the aluminum or conductive fabric is used as top electrodes to connect with the prepared LPPS-NFC film separated by a spacer, establishing a hybrid TPENG device to collect mechanical energy from diverse biomechanical movements.

The unit cell of Cs₃Bi₂Br₉ is shown in **Figure 1a**. Cs₃Bi₂Br₉ has a hexagonal structure, and one cesium atom is surrounded by six bismuth bromide octahedral frameworks. **Figure 1b** displays the powder X-ray diffraction (XRD) patterns of Cs₃Bi₂Br₉, which match well with the standard PDF card (44-0714),



Scheme 1. Conceptual demonstrations of LPPS-NFC for energy harvesting from various human motions, and a schematic illustration of the fabrication process of an LPPS-NFC-based TPENG device.

confirming the excellent phase purity and crystallinity. The scanning electron microscopy (SEM) images presented in Figure 1c clearly show the hexagonal structures of $\text{Cs}_3\text{Bi}_2\text{Br}_9$ perovskites, which is consistent with the unit cell in Figure 1a, further affirming the lattice structures of $\text{Cs}_3\text{Bi}_2\text{Br}_9$ perovskites.

The hydrophobicity and breathability of $\text{Cs}_3\text{Bi}_2\text{Br}_9$ -embedded LPPS-NFC films are also investigated in detail. As depicted in Figure 1d, the contact angle of the LPPS-NFC with 1 wt% $\text{Cs}_3\text{Bi}_2\text{Br}_9$ is 135.8° because of the intrinsic hydrophobicity of SEBS and PVDF-HFP. The photographs and contact angles for the LPPS-NFCs with different $\text{Cs}_3\text{Bi}_2\text{Br}_9$ contents are shown in Figures S1 and S2 in the Supporting Information. All these films show good hydrophobicity with similar contact angles (132° – 136°). The LPPS-NFC also displays great electrostatic adhesion with different materials such as curved glass or stainless steel (Figure 1e), suggesting that it not only conforms tightly with human skin or clothes, but also attaches to different objects to fit various application scenarios. Moreover, LPPS-NFC exhibits outstanding breathability derived from the pores among the nanofibers, which can be estimated by calculating the water vapor transmittance (WVT) based on the Fickian diffusion ($\text{WVT} = (m_2 - m_1)/A$, where A is the surface area, and m_1 and m_2 are the weights of the bottle with water before and after the test). As shown in Figure 1f, the LPPS-NFC films display large WVT rates ($\approx 10 \text{ kg m}^{-2} \text{ d}^{-1}$) and only experience a slight decrease when the $\text{Cs}_3\text{Bi}_2\text{Br}_9$ content is larger than 2 wt%, demonstrating great breathability compared to other nanofiber composites (WVT rates of polyurethane/sodium chloride, fluorinated polyurethane/silica, and polyurethane/hydrophobic silica gel fibrous membranes are 9.06, 6.91, and $8.05 \text{ kg m}^{-2} \text{ d}^{-1}$, respectively).^[52–54]

Apart from the excellent waterproof and breathability, the LPPS-NFC also exhibits a high stretchability owing to the addition of SEBS binders. As shown in the SEM images

(Figure 1g and Figures S3 and S4, Supporting Information), the LPPS-NFC films display a clear distribution of SEBS local microspheres (highlighted by orange circles), which was early found in our previous publication.^[55] When stretching the LPPS-NFC films, these microspheres not only bind and interlock the PVDF-HFP/ $\text{Cs}_3\text{Bi}_2\text{Br}_9$ nanofibers to restrain their further physical sliding, but also deform to sustain the stretching force, endowing the LPPS-NFC with a good stretchability of over 500% (Figure 1h). It is worth noting that both the stretchability and tensile strength are enhanced when the $\text{Cs}_3\text{Bi}_2\text{Br}_9$ content is lower than 2 wt%, while higher $\text{Cs}_3\text{Bi}_2\text{Br}_9$ content ($>2 \text{ wt}\%$) weakens the stretching performance. This is because most $\text{Cs}_3\text{Bi}_2\text{Br}_9$ gets incorporated into PVDF-HFP nanofibers when the perovskite content is low (Figure 2b), and they can serve as nucleation sites and offer extra ionic interaction force with PVDF-HFP which can alleviate the growth of cracks and fractures during the stretching process, leading to better stretchability and tensile strength.^[44,56] In contrast, excessive perovskites ($>2 \text{ wt}\%$) could wrap or cover the nanofibers (Figure 2c), which increase the mechanical stiffness of PVDF-HFP, rendering the LPPS-NFC films to become more brittle.^[44] The detailed mechanical properties, such as Young's modulus as well as tensile strength and strain, of the different LPPS-NFC films are also summarized according to the tensile curves, which are displayed in Table S1 in the Supporting Information. The LPPS-NFC film (1 wt% $\text{Cs}_3\text{Bi}_2\text{Br}_9$) also shows great recovery according to tensile stress–strain cycling tests (200%), suggesting the good energy dissipation ability of the elastic network (Figure 1i). The cycling tests for different stretchabilities (50%, 100%, 150%, and 200% strain) and stretching speeds (50, 100, and 150 mm min^{-1}) are also investigated (Figures S5 and S6, Supporting Information). All the tests show great recovery performance of LPPS-NFC, indicating its excellent stretching durability and stability.

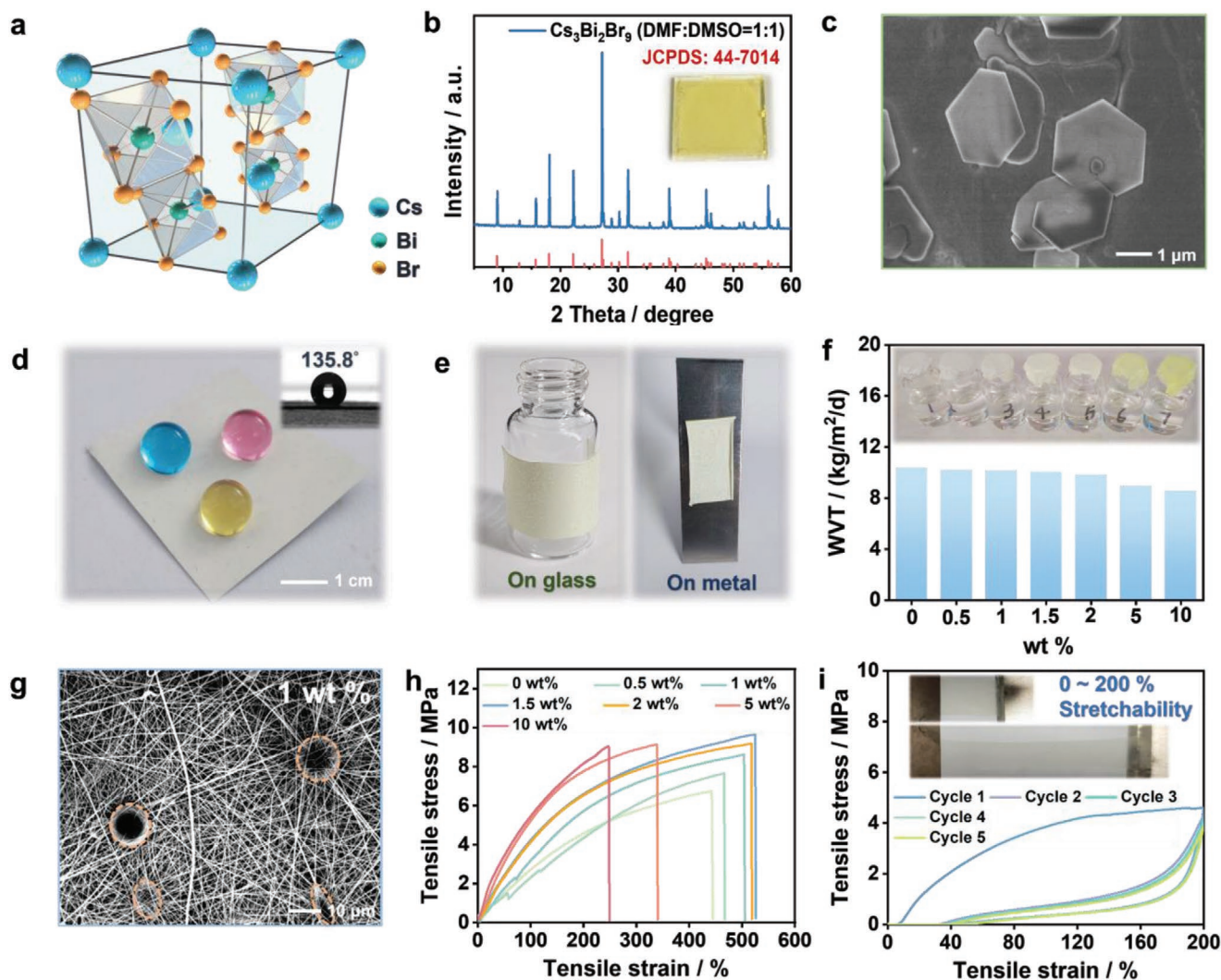


Figure 1. a) Unit cell crystal structures of $\text{Cs}_3\text{Bi}_2\text{Br}_9$. b) XRD patterns of $\text{Cs}_3\text{Bi}_2\text{Br}_9$. Inset: The $\text{Cs}_3\text{Bi}_2\text{Br}_9$ thin film. c) SEM images of pure $\text{Cs}_3\text{Bi}_2\text{Br}_9$ thin film. d) Photographs of LPPS-NFC film (1 wt% $\text{Cs}_3\text{Bi}_2\text{Br}_9$) with good hydrophobic properties. Inset: The water contact angle of LPPS-NFC is 135.8° . e) The good adhesion of LPPS-NFC with curved glass and metal substrate. f) A comparison of water vapor transmittance rates of LPPS-NFC with different $\text{Cs}_3\text{Bi}_2\text{Br}_9$ content. g) SEM image of LPPS-NFC film with 1 wt% $\text{Cs}_3\text{Bi}_2\text{Br}_9$. The SEBS microspheres are clearly shown in the image. h) Tensile stress–strain curves of the LPPS-NFC with different $\text{Cs}_3\text{Bi}_2\text{Br}_9$ contents. i) Cyclic tensile stress–strain curves of the LPPS-NFC with 1 wt% $\text{Cs}_3\text{Bi}_2\text{Br}_9$. Inset: Photographs of LPPS-NFC (1 wt% $\text{Cs}_3\text{Bi}_2\text{Br}_9$) at 0% and 200% strain.

Figure 2a explains the contributions of perovskites to the electric output performance of LPPS-NFC-based energy harvesters. It has been reported that polycrystalline perovskites usually possess high defects density, which are almost five orders of magnitudes higher than conventional crystalline silicon or single-crystal materials.^[59,60] Typically, these defects may inhibit most applications of perovskites because they are easily affected by the external atmosphere, such as heat, light, moisture, and oxygen.^[41] In view of the strong carrier trapping capacity, these defects will impede the carrier transport processes, especially for the application of solar cell and LED.^[42,61] These defects may play a crucial role in the application of TENG as the defects can serve as efficient electron trapping acceptors to preserve more negative charges and enhance the triboelectric output, which has been proved by both experimental and theoretical investigations.^[50,57] Figure 2d shows

the electron transfer and trapping mechanism of LPPS-NFC-based energy devices during the contact–separation process. According to the tendency to gain or lose electrons in the triboelectric series,^[62] the electrons will transfer from the Al to the lowest unoccupied molecular level of the PVDF-HFP and then be rapidly captured by the $\text{Cs}_3\text{Bi}_2\text{Br}_9$ perovskite considering the narrow energy level difference between PVDF-HFP and perovskites.^[57,63] Compared to other halide perovskites and functional fillers, $\text{Cs}_3\text{Bi}_2\text{Br}_9$ also displays exceptional advantages. As illustrated in Figure 2e, $\text{Cs}_3\text{Bi}_2\text{Br}_9$ shows the best energy level matching with the PVDF-HFP (energy level difference is around 0.3 eV),^[57] which is beneficial to the electron transfer between the two materials, while for other materials, such as MAPbBr_3 ,^[58] FAPbI_3 ,^[58] rGO ,^[36] ZnO ,^[35] and MoS_2 ,^[37] the energy level difference with PVDF-HFP is over 1 eV, which will inhibit the electron transfer process and increase the

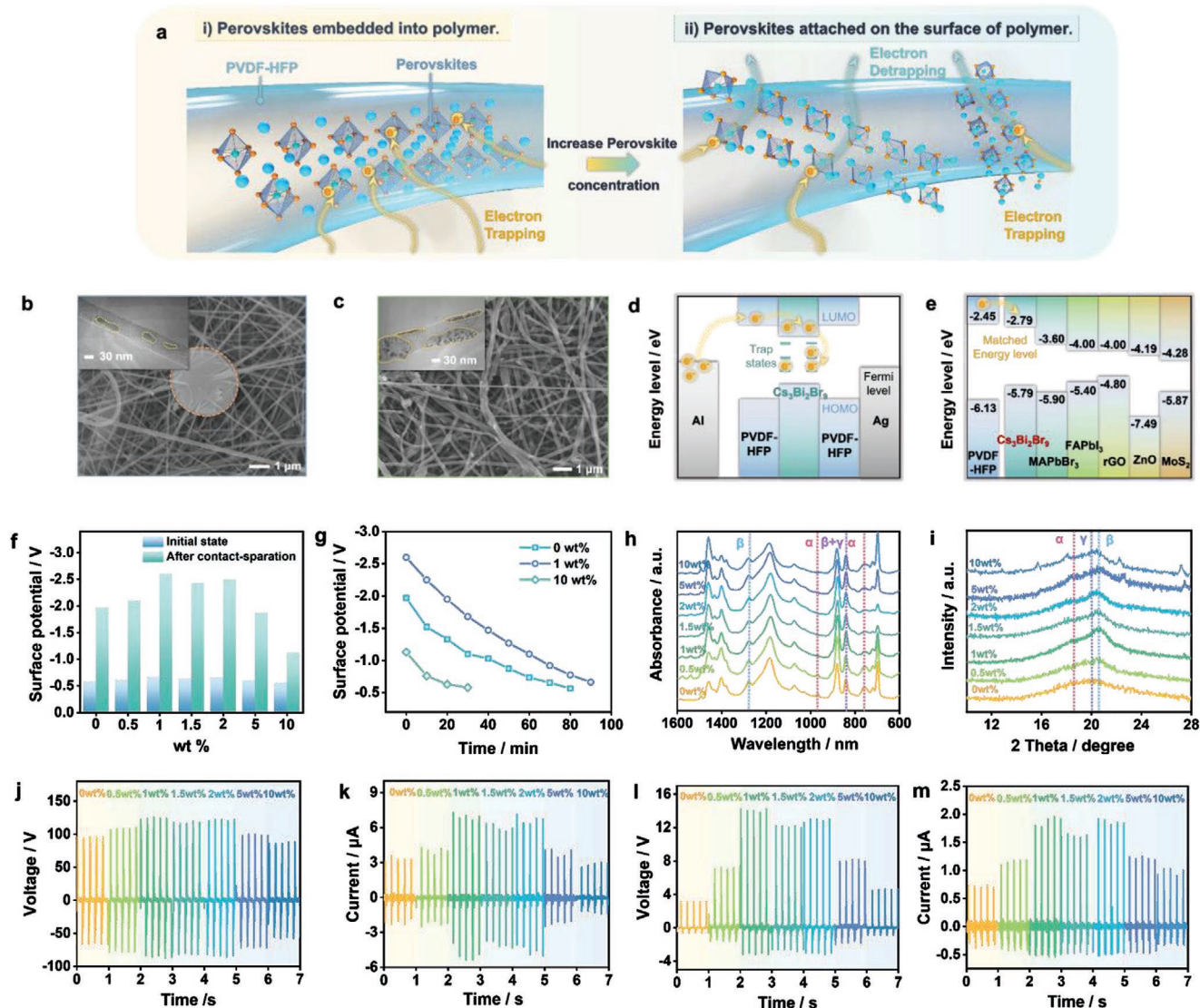


Figure 2. a) Schematic illustration of the contributions of $\text{Cs}_3\text{Bi}_2\text{Br}_9$ to the LPPS-NFC film. i) When most $\text{Cs}_3\text{Bi}_2\text{Br}_9$ is embedded into the LPPS-NFC, the electrons transferred from PVDF-HFP can be well trapped and preserved. PVDF-HFP can reduce the charge dissipation of $\text{Cs}_3\text{Bi}_2\text{Br}_9$. ii) When most $\text{Cs}_3\text{Bi}_2\text{Br}_9$ is attached to the surface of PVDF-HFP, the electrons trapped by the perovskites will be rapidly dissipated through the surface perovskite conductive pathways, due to the exposed defects and semiconducting properties of $\text{Cs}_3\text{Bi}_2\text{Br}_9$. b) SEM image of LPPS-NFC film with 1 wt% $\text{Cs}_3\text{Bi}_2\text{Br}_9$. Inset: Corresponding TEM image of LPPS-NFC film with 1 wt% $\text{Cs}_3\text{Bi}_2\text{Br}_9$. Most perovskites are incorporated into the nanofibers. c) SEM image of LPPS-NFC film with 10 wt% $\text{Cs}_3\text{Bi}_2\text{Br}_9$. Inset: Corresponding TEM image of LPPS-NFC film with 10 wt% $\text{Cs}_3\text{Bi}_2\text{Br}_9$. Most perovskites will wrap and cover the surface of nanofibers as perovskite particles observed in the SEM image. d) Energy level illustration of LPPS-NFC-based device and the corresponding electron transfer and trapping process. e) Energy level illustration of LPPS-NFC-based device and the corresponding energy levels with other materials, such as MAPbBr_3 ,^[58] FAPbI_3 ,^[58] rGO ,^[36] ZnO ,^[35] and MoS_2 .^[37] f) Surface potential of LPPS-NFC films with different $\text{Cs}_3\text{Bi}_2\text{Br}_9$ contents before and after contact-separation with Al (30 N and 5 Hz) obtained from KPFM. g) The retention time of the surface potential of LPPS-NFC films with 0, 1, and 10 wt% perovskites after contact-separation with Al (30 N and 5 Hz). h) FT-IR of LPPS-NFC films with different $\text{Cs}_3\text{Bi}_2\text{Br}_9$ content. i) XRD of LPPS-NFC films with different $\text{Cs}_3\text{Bi}_2\text{Br}_9$ content. j) Output voltage of the LPPS-NFC-based TPENG with different $\text{Cs}_3\text{Bi}_2\text{Br}_9$ content under the test condition of 30 N and 5 Hz. k) Output current of the LPPS-NFC-based TPENG with different $\text{Cs}_3\text{Bi}_2\text{Br}_9$ content under the test condition of 30 N and 5 Hz. l) Output voltage of the LPPS-NFC-based PENG with different $\text{Cs}_3\text{Bi}_2\text{Br}_9$ content under the test condition of 30 N and 5 Hz. m) Output current of the LPPS-NFC-based PENG with different $\text{Cs}_3\text{Bi}_2\text{Br}_9$ content under the test condition of 30 N and 5 Hz.

charge loss,^[38–40] posing a negative impact on the electron trapping process. As a result of the intrinsic defects of $\text{Cs}_3\text{Bi}_2\text{Br}_9$ perovskite, a number of trap states will be distributed between the conduction and valance band (Figure 2d), which can trap and store more electrons. Therefore, the embedded $\text{Cs}_3\text{Bi}_2\text{Br}_9$ perovskites are promising materials that perform as local

electron acceptors and accommodate more electrons, promoting triboelectric output performance.

Furthermore, the contents of $\text{Cs}_3\text{Bi}_2\text{Br}_9$ perovskites embedded into PVDF-HFP also play a vital role in the electric output performance of LPPS-NFC-based energy devices. As shown in SEM and transmission electron microscope

(TEM) images (Figure 2b), no discernable perovskite nanoparticles can be observed around the nanofibers as most of them are embedded into the PVDF-HFP at low perovskite content (≤ 2 wt%). In this case, the PVDF-HFP nanofibers can serve as a protective function in reducing the charge dissipation of perovskites, significantly enhancing both V_{oc} and I_{sc} at low $\text{Cs}_3\text{Bi}_2\text{Br}_9$ content. In contrast, when the content is higher than 5 wt%, $\text{Cs}_3\text{Bi}_2\text{Br}_9$ will form distinct particles or wrap on the surface of nanofibers (as illustrated in Figure 2c), resulting in perovskites being exposed to the ambient environment and affecting the contacts of LPPS-NFC film and electrodes. The semiconducting and ionic properties of the exposed $\text{Cs}_3\text{Bi}_2\text{Br}_9$ perovskite will also accelerate the surface charge dissipation because of its higher electrical conductivity than PVDF-HFP. These factors will degrade the electrical output of LPPS-NFC, leading to a decreased electric performance at higher $\text{Cs}_3\text{Bi}_2\text{Br}_9$ content (≥ 5 wt%).

To further prove the charge trapping mechanism of the LPPS-NFC, surface potential measurements of LPPS-NFC films with various $\text{Cs}_3\text{Bi}_2\text{Br}_9$ contents were conducted using Kelvin probe force microscopy (KPFM) and electrostatic voltmeter. As illustrated in Figure 2f and Figure S8 in the Supporting Information, KPFM results show similar surface potential (≈ -0.6 V) for the LPPS-NFC films with different $\text{Cs}_3\text{Bi}_2\text{Br}_9$ contents at their initial states. After a 10 min contact–separation with Al electrode (30 N, 5 Hz), all the LPPS-NFCs display more negative surface potential due to the charge accumulation. Particularly, LPPS-NFC film with 1 wt% $\text{Cs}_3\text{Bi}_2\text{Br}_9$ exhibits the most negative surface potential (-2.60 V), which is significantly lower than the PVDF-HFP/SEBS nanofiber film without $\text{Cs}_3\text{Bi}_2\text{Br}_9$ (-1.97 V), indicating the incorporated perovskites can trap and maintain the induced electrons. On the contrary, the surface potential of LPPS-NFC (10 wt% $\text{Cs}_3\text{Bi}_2\text{Br}_9$) only reaches -1.13 V, which is dramatically higher than the pure PVDF-HFP/SEBS nanofiber, implying the reduced charge trapping capacity. To evaluate the different charge dissipation mechanisms, three typical LPPS-NFC films (0, 1, and 10 wt%) were selected to investigate their charge loss process. From the results of KPFM (Figure 2g and Figures S9–S11, Supporting Information), the surface potential for LPPS-NFC with 1 wt% perovskite content is -2.60 V after sufficient contact–separation with Al (30 N, 5 Hz) and it can be maintained for around 90 min before returning to the initial value (-0.66 V). Additionally, the potential decay rate of LPPS-NFC film with 1 wt% perovskite content is similar to the PVDF-HFP/SEBS without perovskites, illustrating that the incorporated perovskites are well protected and the charge dissipation process is dominated by the PVDF-HFP. Conversely, the surface potential for LPPS-NFC film with 10 wt% perovskites will rapidly drop from -1.13 to -0.56 V within 30 min, revealing that the exposed perovskites will affect the electron trapping capacity and accelerate the charge loss process. The surface potential measured from the electrostatic voltmeter also shows a similar pattern to the KPFM results (Figure S12, Supporting Information), further confirming the charge trapping and dissipation process of the LPPS-NFCs. To quantitatively compare the charge dissipation process of the LPPS-NFC films, the surface potential decay rates for the first 20 min of LPPS-NFC films with 0, 1, and 10 wt% perovskites are calculated based on the results from the electrostatic voltmeter, which are determined

to be 9.0, 9.2 and 18.4 mV min^{-1} , respectively. Notably, the initial surface potential mainly derives from PVDF-HFP when $\text{Cs}_3\text{Bi}_2\text{Br}_9$ content is lower than 10 wt% due to the limited $\text{Cs}_3\text{Bi}_2\text{Br}_9$ coverage on the surface of PVDF-HFP nanofibers, while it will gradually increase at higher $\text{Cs}_3\text{Bi}_2\text{Br}_9$ content (30 and 50 wt%) and approach to the surface potential of pure $\text{Cs}_3\text{Bi}_2\text{Br}_9$ thin film of 0.37 V, indicating that the $\text{Cs}_3\text{Bi}_2\text{Br}_9$ will be considerably exposed to the external environment and cover the surface of nanofibers, which will prominently influence the surface potential of LPPS-NFC (see Figures S13 and S14 in the Supporting Information for more details). The surface potential measurements provide direct evidence that the embedded perovskites in PVDF-HFP nanofibers can act as efficient electron acceptors to store and enhance the negative charges, confirming our proposed mechanism in Figure 2a.

Apart from the charge trapping capacities, the perovskite-embedded LPPS-NFCs also show significantly enhanced piezoelectric performance. Normally, for polycrystalline PVDF-HFP, polar β and semipolar γ phases (electroactive phases) are mainly responsible for the piezoelectric performance, while other phases, such as nonpolar α and amorphous phases, do not contribute to the piezoelectric properties.^[44,46] Therefore, increasing the proportion of electroactive phases, especially for the polar β phase, is vital to enhance the piezoelectric output of LPPS-NFC. During the ES process, the semiconducting $\text{Cs}_3\text{Bi}_2\text{Br}_9$ perovskites will generate inductive charges under the high electrical field, so a local Coulomb force can be induced to improve in situ poling and β -crystalline formation of piezoelectric polymers,^[44,46] which can be proven by the effective average of the piezoelectric coefficient ($d_{33, \text{eff}}$), Fourier transform infrared (FT-IR) spectra, XRD, and differential scanning calorimetry (DSC) measurements. From the FT-IR results (Figure 2h and Table S3, Supporting Information), some vibrational peaks represent different phases, including nonpolar α -phase (764 and 975 cm^{-1}), polar β -phase (1277 cm^{-1}), and superimposed β - and γ -phase (841 cm^{-1}). LPPS-NFC with 1 wt% $\text{Cs}_3\text{Bi}_2\text{Br}_9$ exhibits the highest electroactive phase of 77%, whereas pure PVDF-HFP/SEBS composite can only reach 55% electroactive phase. XRD tests are also conducted to confirm the crystalline features of LPPS-NFCs (Figure 2i). The diffraction peaks at 18.4° , 20.2° , and 20.8° represent the α -, γ -, and β -phase of PVDF-HFP, respectively. To quantitatively compare the different crystalline phases of the LPPS-NFCs with different $\text{Cs}_3\text{Bi}_2\text{Br}_9$ contents, peak fitting is utilized to calculate their respective phase fraction (as shown in Figure S16 and Table S4, Supporting Information). Based on the XRD results, the LPPS-NFC with 1 wt% $\text{Cs}_3\text{Bi}_2\text{Br}_9$ shows 70.4% total crystalline and 52.4% β -crystalline phase, which is higher than pure PVDF-HFP/SEBS films (45.9% total crystalline phase and 17.2% β -crystalline phase). Notably, the further increment of $\text{Cs}_3\text{Bi}_2\text{Br}_9$ will decrease the peak intensity of β -crystalline phase. Moreover, some additional peaks appear when the $\text{Cs}_3\text{Bi}_2\text{Br}_9$ content reaches 10 wt%, which can be assigned to the characteristic peaks of $\text{Cs}_3\text{Bi}_2\text{Br}_9$, verifying that $\text{Cs}_3\text{Bi}_2\text{Br}_9$ has been exposed to the ambient environment at high content. DSC results also display a similar relationship between perovskite content and crystalline phase, as illustrated in Figure S17 and Table S5 in the Supporting Information. Based on the DSC curves, the LPPS-NFC with 1 wt% $\text{Cs}_3\text{Bi}_2\text{Br}_9$ also exhibits

the highest crystalline phase fraction (71.1%) compared to pure PVDF-HFP/SEBS nanofiber composite (41.8%), and the crystalline features of LPPS-NFCs match well with the XRD results. Hence, FT-IR, XRD, and DSC analyses all show the same change patterns of crystalline phase and β -phase fraction, confirming that moderate $\text{Cs}_3\text{Bi}_2\text{Br}_9$ content can dramatically promote the crystalline process and enhance the β -phase crystallization of PVDF-HFP.

To further verify the triboelectric and piezoelectric enhancement mechanism of $\text{Cs}_3\text{Bi}_2\text{Br}_9$ perovskites, a stretchable and breathable LPPS-NFC was prepared and optimized to obtain the best electrical performance. The weight ratio of PVDF-HFP/SEBS was selected as 3:7 which has been confirmed with the optimal stretchable and triboelectric performance shown in our previous work.^[55] Then the LPPS-NFCs with various $\text{Cs}_3\text{Bi}_2\text{Br}_9$ contents from 0 to 10 wt% were used to fabricate TPENG devices to evaluate their electrical output. Figure S7a in the Supporting Information shows the schematic structure of a TPENG device, where an LPPS-NFC film ($2 \times 2 \text{ cm}^2$) is attached to a conductive fabric, and an aluminum foil serving as the friction and conductive layer. The LPPS-NFC/conductive fabric and Al foil are fixed on two different polyethylene terephthalate substrates and separated by a spacer of 2 mm VHB tape. The electrical experiment is conducted under a force of 30 N and a frequency of 5 Hz. As shown in Figure 2j,k, the output open-circuit voltage (V_{oc}) and short-circuit current (I_{sc}) of the TPENG devices increase by about 30% and 118% when the $\text{Cs}_3\text{Bi}_2\text{Br}_9$ contents rise from 0 to 1 wt%, while excessive $\text{Cs}_3\text{Bi}_2\text{Br}_9$ content (>2 wt%) will reduce the electrical output. These results confirm that the addition of moderate $\text{Cs}_3\text{Bi}_2\text{Br}_9$ contents can significantly enhance the electrical output performance of LPPS-NFC film.

To prove the enhanced β -phase can promote the piezoelectric output performance, the LPPS-NFC-based PENG devices ($2 \times 2 \text{ cm}^2$) with different $\text{Cs}_3\text{Bi}_2\text{Br}_9$ content were also fabricated (Figure S7b, Supporting Information). Under the experimental condition of 30 N and 5 Hz, the piezoelectric output of LPPS-NFC film with 1 wt% $\text{Cs}_3\text{Bi}_2\text{Br}_9$ shows an apparent electrical enhancement ($\approx 17 \text{ V}$, $\approx 2.5 \mu\text{A}$) compared to pure PVDF-HFP/SEBS films ($\approx 3 \text{ V}$, $\approx 1 \mu\text{A}$) as displayed in Figure 2l,m. However, the electrical output will drop to $\approx 5 \text{ V}$ and $\approx 1.2 \mu\text{A}$ when the $\text{Cs}_3\text{Bi}_2\text{Br}_9$ content increases to 10 wt%. This is because the exposed perovskites will impede the crystallization of PVDF-HFP. In addition, the dipoles of PVDF-HFP will be pinned by the defects or the surface charges at the interface between the exposed $\text{Cs}_3\text{Bi}_2\text{Br}_9$ and PVDF-HFP nanofibers, leading to the decreasing polarization and low piezoelectric output of the LPPS-NFC.^[64] The inversed signals are also observed when the device connection is reversed, further demonstrating that the electrical output comes from the piezoelectric effect (Figure S15, Supporting Information). To exclude the potential piezoelectric influence of $\text{Cs}_3\text{Bi}_2\text{Br}_9$, free-standing $\text{Cs}_3\text{Bi}_2\text{Br}_9$ thin film is also prepared (details can be found in the Experimental Section), and no piezoelectricity was detected ($d_{33,eff} = 0$). Hence, the piezoelectricity of LPPS-NFC mainly derives from PVDF-HFP nanofibers. Table S2 in the Supporting Information summarizes the $d_{33,eff}$ of diverse LPPS-NFCs, which are consistent with the piezoelectric output results, providing direct evidence to the piezoelectric enhancing functions of $\text{Cs}_3\text{Bi}_2\text{Br}_9$.

To obtain higher power output and adapt to various application scenarios, we design stretchable and breathable LPPS-NFCs for hybrid TENG and PENG energy harvesters (TPENGs) and investigate their force- and frequency-dependent electric output performances. The working mechanism of LPPS-NFC-based TPENG is illustrated in Figure 3a. The LPPS-NFCs act as both tribo- and piezoelectric layers, and the Al serves as electrode and another triboelectric layer. Initially, the LPPS-NFC and Al are separated from each other, and the device is electrically neutral. When the two materials are in contact, the electrons will be transferred from Al to the LPPS-NFC, such that the triboelectric negative and positive charges are induced in LPPS-NFC and Al, respectively. Meanwhile, LPPS-NFC will experience deformation due to the external compression, and therefore, a built-in piezoelectric potential is generated within the LPPS-NFC. To balance the potential, the negative charge will flow from the top to the bottom electrode through the external load. When the compression force is released, the negative charge will flow back to maintain the electrostatic neutral state of the LPPS-NFC. In the meantime, the triboelectric negative charges will also flow in the same direction to balance the triboelectric potential due to the separation of two materials. Afterward, when the external force is applied to the device again, the Al will approach the LPPS-NFC, and the electrons will flow from the top to the bottom electrode again, then the circulation will continue in the same way. According to the working mechanism of the LPPS-NFC-based TPENG, the triboelectric and piezoelectric charges flow in the same direction almost at the same time, so both of them contribute to the enhancement of electrical output.

To guarantee the breathability and stretchability of LPPS-NFC-based TPENG devices, a printable Ag electrode is used as the top electrode. This Ag electrode can form dense microflakes on spandex that can not only maintain its high conductivity, but also offer printable and stretchable properties (Figure 3b). This conductive Ag electrode can be printed as multifarious patterns that exhibit excellent adhesion with spandex and can be adapted to different application scenarios (inserted image of Figure 3d).^[55,65] As displayed in Figure 3c, the Ag-SEBS ink with 2:1 weight ratio exhibits the best conductivity under the stretching state, which is below 5Ω even at 100% strain. In addition, the Ag-SEBS ink (2:1, w/w) also shows excellent cycling stability (Figure 3d and Figure S18, Supporting Information), which can be used as an ideal conductive electrode for breathable and stretchable LPPS-NFC-based TPENG devices.

Based on the above stretchable Ag electrodes, LPPS-NFC-based TPENG devices ($3 \times 4 \text{ cm}^2$) were fabricated to investigate their electrical output (voltage, current, and transferred charge) under different forces and frequencies. The cross-section SEM image of the device is shown in Figure S19 in the Supporting Information, where the thickness of the silver electrode and LPPS-NFC film is around 20 and $4 \mu\text{m}$, respectively. As shown in Figure 3e-j, the current and transferred charge increase with the growth of force and frequency. The voltage also increases with increasing the force and reaches the highest when the frequency equals to 7 Hz. The increasing output voltage with frequency is mainly due to the excellent charge trapping capacity of the LPPS-NFC. When the frequency

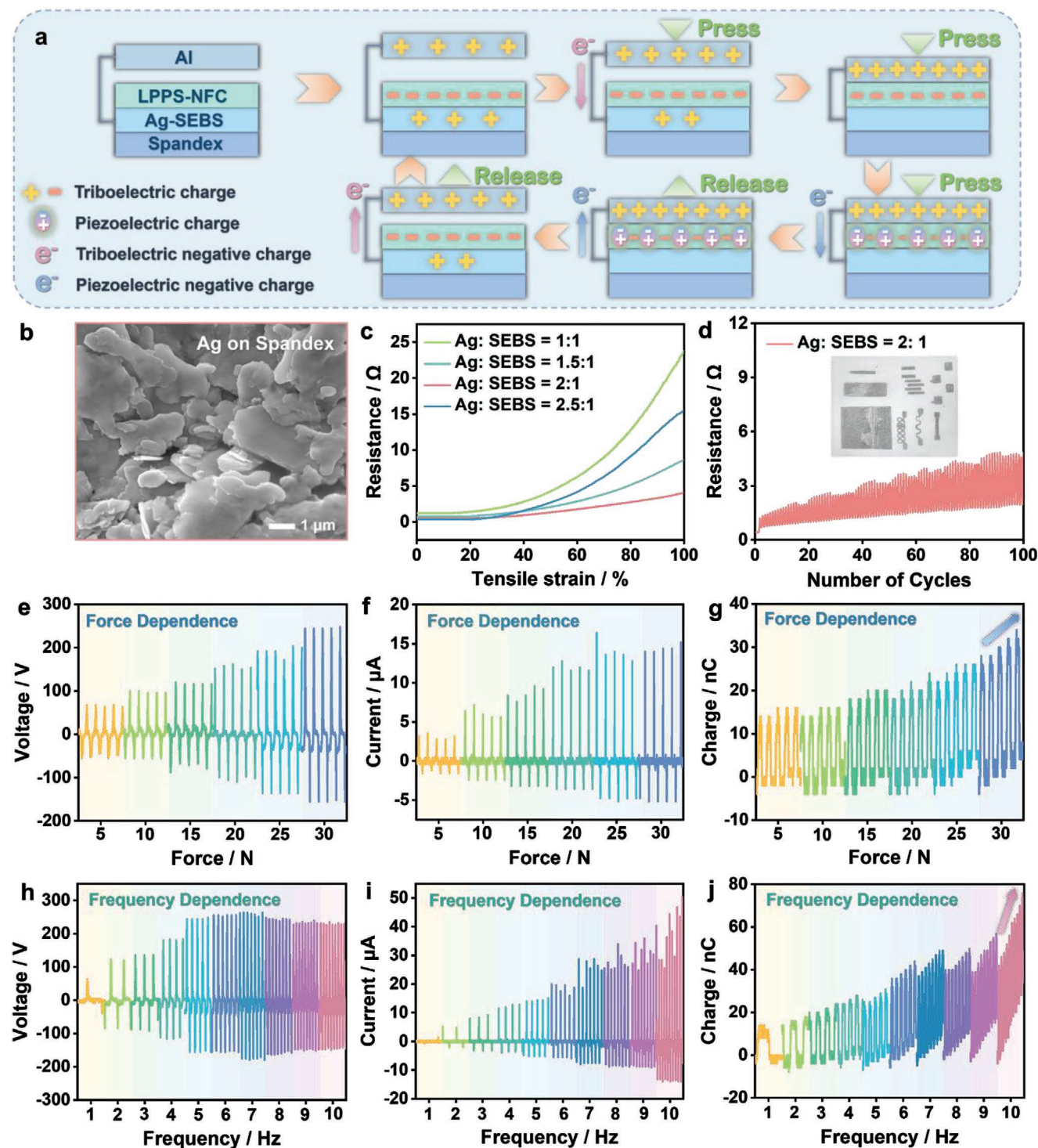


Figure 3. a) Working principle of LPPS-NFC-based TPENG device. b) SEM image of Ag-SEBS electrode on spandex substrate. c) Ratio optimization of the Ag-SEBS electrode under 100% tensile strain. d) Cycling stability tests of the Ag-SEBS electrode with 2:1 weight ratio. Inset: Different patterns of the Ag-SEBS electrode through screen printing. e–g) Force-dependent electrical performance (voltage, current, and transferred charge) measurements of LPPS-NFC with 1 wt% $\text{Cs}_3\text{Bi}_2\text{Br}_9$. h–j) Frequency-dependent electrical performance (voltage, current, and transferred charge) measurements of LPPS-NFC with 1 wt% $\text{Cs}_3\text{Bi}_2\text{Br}_9$.

is lower than 7 Hz, the strong charge trapping capacity will promote the electrostatic charges to rapidly accumulate at the surface of the LPPS-NFC, leading to more induced charges

accumulating on the electrode; thus, the output voltage will increase with the frequency.^[66–68] The reduced output voltage for higher frequencies (>7 Hz) is attributed to the restricted

charge transfer considering the transient contact. The insufficient contacts between the LPPS-NFC and Al will impede the charge transfer and accumulation process on the electrode, so the output voltage will slightly reduce. This result was also observed by other studies including both TENG and PENG applications,^[34,45,55,69,70] which can further support our experimental result. Under the condition of 30 N at 5 Hz, the generated voltage and current density were 400 V and 1.63 $\mu\text{A cm}^{-2}$, respectively. To the best of our knowledge, the output voltage is the highest value among all the reported halide-perovskite-based mechanical energy harvesters (a comparison among the state-of-art halide-perovskite-based mechanical energy harvesters is summarized in Tables S6 and S7, Supporting Information).^[33,68,71–74] The transferred charge is around 30 nC at the initial stage, and it will gradually increase with time due to the charge accumulation, further confirming that LPPS-NFCs have excellent charge trapping capacity. The power output of the LPPS-NFC-based TPENG devices was also investigated by varying the different load resistors. As depicted in Figure S20 in the Supporting Information, the output voltage will increase with the growth of load resistors, while the current will decrease with the increment of resistance. The maximum power output of 2.34 W m^{-2} is achieved when the resistance reaches 20 $\text{M}\Omega$, which is over ten times higher than the pure PVDF-HFP/SEBS films reported in our previous work (219.66 mW m^{-2}).^[55] Apart from the excellent electrical output performance, the humidity-resistance property of the device was also investigated in the same experimental condition (30 N, 5 Hz, 20 $\text{M}\Omega$). The LPPS-NFC-based TPENG was fixed in a sealed system and the humidity was controlled by the silica gel (moisture absorbent) and commercial humidifier. As illustrated in Figure S21 in the Supporting Information, the electrical output of the LPPS-NFC-based TPENG devices can maintain a stable value under different humidity (50–99%); the output voltage, current, and power density only reduce by 8%, 5%, and 16%, respectively, which are comparable or even better than some other humidity-resistant TENG devices.^[75,76] The excellent humidity-resistant property is derived from the intrinsic nanostructure and high surface roughness of nanofibers as well as outstanding hydrophobic nature of PVDF-HFP and SEBS, rendering the LPPS-NFC-based TPENG to become promising devices for wearable electronics and smart textiles.

In view of the outstanding flexibility and adaptability of energy harvesters, LPPS-NFC can be designed as TPENG and PENG to satisfy different application scenarios. As shown in Figure 4a, the LPPS-NFC-based TPENG and PENG were attached to the top and bottom side of a shoe pad for collecting the energy from walking or running. The bottom PENG device can collect the piezoelectric energy during the stomping process, while at the same time, the contact and separation between the heel and top TPENG device allow the energy harvesting from both triboelectric and piezoelectric energy. Hence, the well-designed device structure with good breathability and waterproofness can simultaneously harvest energy from both piezoelectric and triboelectric energy, contributing to the high output voltage of ≈ 17 and ≈ 290 V for PENG and TPENG, respectively (Figure 4b,c). Figure 4d demonstrates the stretchability and water repellency of LPPS-NFC-based devices, which can bear 50% strain without damage and fracture. The

output voltage of the device will also steadily increase with the tensile strain from 0% to 50% (Figure 4e). This is because the loose and random PVDF-HFP nanofibers will be stretched to be tighter and more aligned under high tensile strain, promoting the compactness of the film surface and the effective contacts with the other triboelectric layer during the contact-separation process, which is consistent with our previous study.^[55] Due to the higher surface compactness of nanofibers and more effective contacts under high tensile strain, the perovskites embedded in PVDF-HFP nanofibers can play a more effective role in charge trapping process on the surface of membranes, thus contributing to the larger surface charge density and also higher output voltage. The current and transferred charges under 0%, 25%, and 50% strain are also demonstrated in Figure 4f,g, showing the gradual electrical increase with the enhanced tensile strain due to the expanded contact area. The LPPS-NFC-based TPENG devices also exhibit excellent resistance to various deformations, such as folding, crumpling, and washing (Figure 4h). After experiencing these harsh treatments, the electrical performance can still keep stable without distinct output decline compared to the original state (Figure 4i). To evaluate the convenience and comfortability of the device, the LPPS-NFC-based TENGs are also prepared and attached to different parts of the human body, such as arm, leg, hand, and elbow (Figure 4j). The devices are easily actuated by tapping or clapping process without affecting the normal activities, revealing their potential advantages as self-powered textiles for wearable electronics. The rectifier bridges are also adopted to transform the alternating current generated by the device to the direct current (Figure 4l), and then drive ≈ 100 LEDs and charge different capacitors (1–100 μF) (Figure 4k,m). Finally, the durability and stability of LPPS-NFC-based TPENG devices are evaluated. Figure 4n,o and Figure S22 in the Supporting Information demonstrate that the LPPS-NFC-based TPENG can maintain long-term durability for 10 000 continuous cycles (30 N, 5 Hz) and also sustain excellent electrical performance for over 5 months. To the best of our knowledge, this is the first hybrid-perovskite-based energy device that concurrently possesses stretchability, breathability, waterproofness, stability as well as outstanding electrical output performance (see Tables S6 and S7 in the Supporting Information for more details), showing the great potential as stable energy harvesters for long-term wearable applications.

3. Conclusion

Stretchable, waterproof, breathable, and stable lead-free halide perovskites/polymers nanofiber composites have been designed to leverage, simultaneously, triboelectric and piezoelectric effects, for energy harvesting. The incorporated $\text{Cs}_3\text{Bi}_2\text{Br}_9$ perovskites not only promote the charge trapping capacity of the nanofiber composite, but also function as additives to improve the polar crystalline phase of PVDF-HFP. The outstanding energy level matching between the $\text{Cs}_3\text{Bi}_2\text{Br}_9$ and PVDF-HFP also increases the charge transfer efficiency and reduces the charge loss, further contributing to the electron-trapping capacity of the LPPS-NFC; thus both triboelectric and piezoelectric output have been greatly enhanced. The excellent

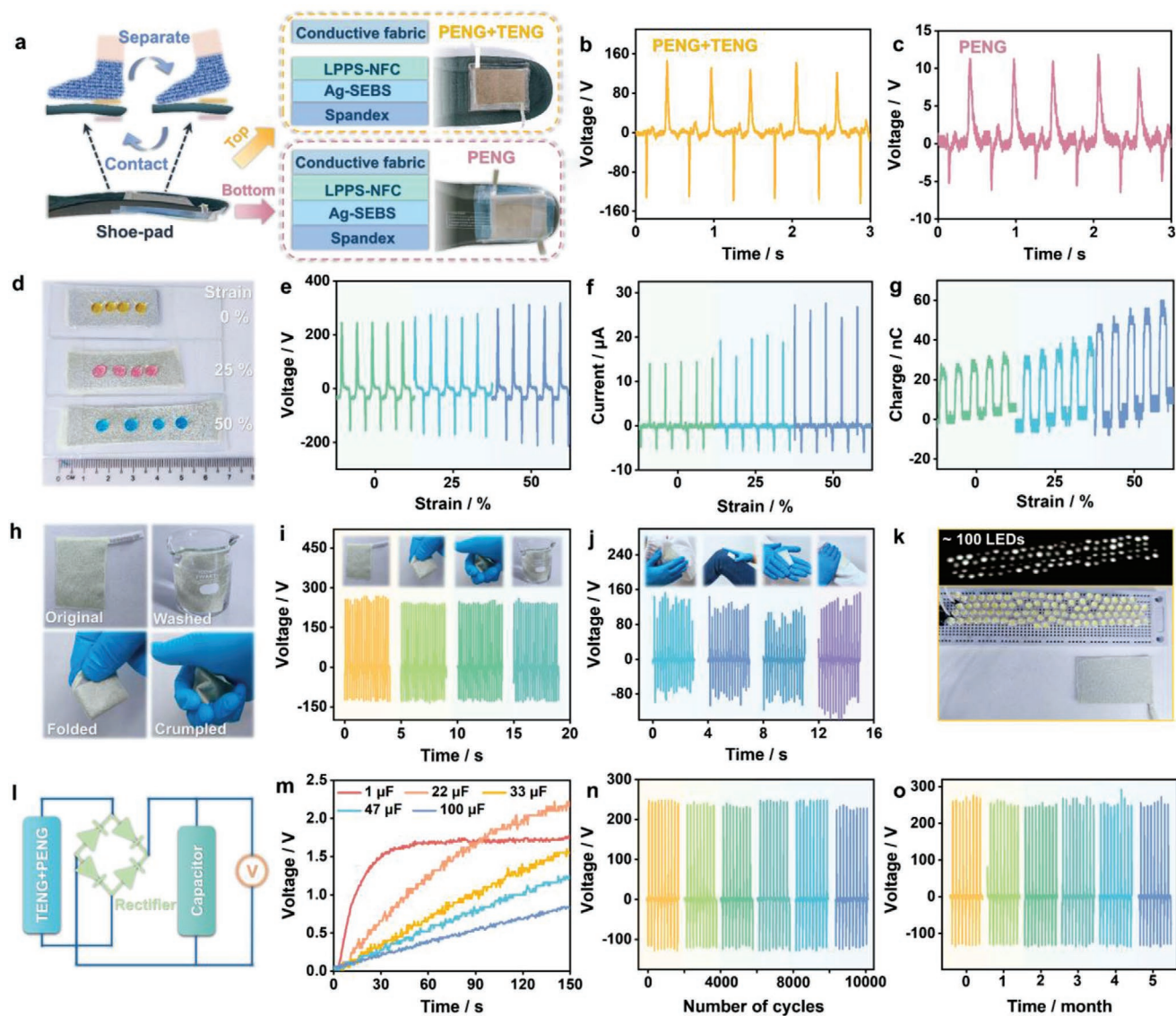


Figure 4. a) Schematic illustration of the LPPS-NFC-based TPENG and PENG devices attached on the shoe-pad actuated by the foot stamping. b,c) The output voltage of the LPPS-NFC-based TPENG (b) and PENG (c). d) Stable water repellency of LPPS-NFC-based devices under different stretching states. e–g) The output voltage, current, and transferred charges of LPPS-NFC-based TPENG under 0%, 25%, and 50% strain. h) Photograph illustrating that the LPPS-NFC-based TPENG owns great endurance for various deformations of washing, folding, and crumpling. i) Output voltage of LPPS-NFC-based TPENG under different deformations. j) Output voltage of LPPS-NFC-based TPENG attached on different body regions. k) LPPS-NFC-based TPENG drives ≈ 100 LEDs by tapping. l) Circuit demonstration for the LPPS-NFC-based TPENG working as a power source. m) The charging process of the LPPS-NFC-based TPENG for different capacitors. n) Output durability of the LPPS-NFC-based TPENG. o) Output stability evaluation of the LPPS-NFC-based TPENG under different months.

electric output of LPPS-NFC enables the conversion of the mechanical energy from different human motions, into the electrical power that can drive common electronic devices, such as LEDs and capacitors. Furthermore, the LPPS-NFC-based energy devices also show good durability and stability, and therefore, can experience extreme mechanical deformations (washing, folding, and crumpling) and long-term continuous tests. The devices can maintain stable electrical performance for up to 5 months, indicating their great potential for long-standing wearable applications. The LPPS-NFC demonstrated here offers an insight into the unique contributions of halide perovskites to the energy devices and also provides a promising

material for energy harvesters, opening up a fresh avenue for self-powered textiles and wearable electronic devices.

4. Experimental Section

Materials: Bismuth bromide (BiBr_3), cesium bromide (CsBr), PVDF-HFP ($M_w \approx 455000$), *N,N*-dimethylformamide (DMF), and dimethyl sulfoxide (DMSO) were purchased from Sigma-Aldrich. All chemicals were used as received without further purification.

Synthesis of $\text{Cs}_3\text{Bi}_2\text{Br}_9$ Perovskites: The precursor solution for $\text{Cs}_3\text{Bi}_2\text{Br}_9$ perovskites was prepared by dissolving CsBr (0.09 mol L^{-1}) and BiBr_3 (0.06 mol L^{-1}) in a mixed solution (DMSO:DMF = 1:4). Then the

Cs₃Bi₂Br₉ films were prepared by dropping the solution on a cleaned glass. After annealing under 60 °C, the pure Cs₃Bi₂Br₉ films were formed on the glass substrate.

Preparation of Free-Standing Cs₃Bi₂Br₉ Thin Film: The precursor solution for Cs₃Bi₂Br₉ perovskites was prepared by dissolving CsBr (0.09 mol L⁻¹) and BiBr₃ (0.06 mol L⁻¹) in a mixed solution (DMSO:DMF = 1:4). Then 100 mL precursor solution was used to obtain pure Cs₃Bi₂Br₉ particles via rotary evaporation under 70 °C. The Cs₃Bi₂Br₉ particles were further ground into fine powder using agate mortar. Finally, ≈100 mg Cs₃Bi₂Br₉ fine powder was utilized to prepare a circular thin film under high mechanical pressure. The diameter of the Cs₃Bi₂Br₉ thin film is around 1.2 cm and the thickness of the film is around 180–220 μm (determined using a micrometer). A mask was utilized to deposit the gold electrode on both sides of the Cs₃Bi₂Br₉ thin film via a sputtering method. Finally, the Cs₃Bi₂Br₉ thin film was poled under 1 kV for 2 h.

Fabrication of the LPPS-NFC Films: LPPS-NFC film was prepared by electrospinning of Cs₃Bi₂Br₉/PVDF-HFP and SEBS simultaneously. The SEBS was dissolved in a mixed solvent (8.5:1.5, v/v) of mesitylene and DMF under the stirring at 50 °C for overnight to obtain the 12 wt% solution. The PVDF-HFP was dissolved in pure DMF and stirred at room temperature for 8 h to prepare 12 wt% solution. After obtaining the pure PVDF-HFP solution, Cs₃Bi₂Br₉ precursor solution with different perovskite concentrations was also prepared and then added to the PVDF-HFP solution to obtain the mixed Cs₃Bi₂Br₉/PVDF-HFP solution (0–10 wt% perovskite contents). The Cs₃Bi₂Br₉ perovskites can be in situ formed with PVDF-HFP nanofibers in the solution state during the electrospinning process, realizing highly homogenous LPPS-NFC composite films. All the LPPS-NFC films were obtained by simultaneous electrospinning of Cs₃Bi₂Br₉/PVDF-HFP and SEBS under 20 kV voltage, and the jet velocities were set as 0.9 and 2.1 mL h⁻¹, respectively. The distance between the nozzle and collector was set to 15 cm and the scanning displacement of the nozzle was set to 5 cm.

Fabrication of the Ag–SEBS Ink: The silver flakes (10 μm) purchased from Sigma-Aldrich were utilized as conductors. The SEBS (TuftecH1052) solution with 100 mg mL⁻¹ concentration was prepared by dissolving them into toluene. Then different weight percents of silver flakes were added into the SEBS solution and stirred for 1 h to obtain the Ag–SEBS electrode ink.

Fabrication of the LPPS-NFC-Based Energy Harvesters: First, the spandex with silver electrode (3 × 4 cm²) was fixed on the collector, then in situ electrospinning was conducted to bind the LPPS-NFC on the electrode tightly. For TENG, the current device can be directly used driven by hand tapping. For the PENG, a conductive fabric/Al with 3 × 4 cm² area was attached on the top as another electrode to form a complete piezoelectric device. For the TPENG devices, the conductive fabric/Al was also added to the top but separated by a spacer to harvest energy from both tribo- and piezoelectric energy.

Characterization of the LPPS-NFC Films: A field-emission SEM (FE-SEM, JEOL 7600F) was utilized to characterize the morphologies of the LPPS-NFC films and electrodes. The FT-IR spectrometer (PerkinElmer Frontier) and powder X-ray diffractometer (XRD, Shimadzu XRD 7000) were utilized to determine the crystallographic phase and structure of the materials. Static contact angle of LPPS-NFC films was tested by an optical contact angle measuring system (Dataphysics OCA15 Pro). Tensile test samples were prepared according to ASTM D638-14 and the stress–strain curves were measured via MTS criterion model 43 (MTS Systems Corporation, Eden Prairie, MN, USA). Young's modulus was obtained from the slope of tensile curves from 0% to 10% strain for each sample. The surface potential of LPPS-NFC was measured by KPFM (Park Systems NX10) and Electrostatic Voltmeter (Trek, Model 542A). The piezoelectric coefficient of the samples was measured by a standard static piezoelectric constant measuring equipment (Sinocera YE2730). The resistances of the stretchable conductors were measured by a Keithley 2400 source meter. The output voltage and applied force were measured by a mixed system of oscilloscope (Tektronix MDO3024, impedance = 100 MΩ) and force transducer (SINOCERA CLYD-331). The output current and transferred charge were recorded by the low-noise current preamplifier (Stanford Research System, model SR570,

impedance = 4 Ω) and Keithley 6517B system, respectively. This work was approved by the Institutional Review Board (IRB) at Nanyang Technological University (IRB-2017-08-038). All the experiments involving human motions were conducted with the agreements of volunteers.

Supporting Information

Supporting Information is available from the Wiley Online Library or from the author.

Acknowledgements

This work was supported by the Ministry of Education (MOE) Singapore, AcRF Tier 1 (Award no. RT15/20). F.J. acknowledges the research scholarship awarded by Institute of Flexible Electronics Technology of Tsinghua, Zhejiang (IFET-THU), Nanyang Technological University (NTU), and Collaborative Innovation Center for Flexible Electronics Technology, China (CICFE).

Conflict of Interest

The authors declare no conflict of interest.

Data Availability Statement

The data that support the findings of this study are available from the corresponding author upon reasonable request.

Keywords

charge trapping, lead-free perovskites, nanogenerators, wearable electronics

Received: January 3, 2022

Revised: February 16, 2022

Published online:

- [1] X. Peng, K. Dong, C. Ye, Y. Jiang, S. Zhai, R. Cheng, D. Liu, X. Gao, J. Wang, Z. L. Wang, *Sci. Adv.* **2020**, *6*, eaba9624.
- [2] Z. Li, M. Zhu, J. Shen, Q. Qiu, J. Yu, B. Ding, *Adv. Funct. Mater.* **2020**, *30*, 1908411.
- [3] D. Yan, J. Chang, H. Zhang, J. Liu, H. Song, Z. Xue, F. Zhang, Y. Zhang, *Nat. Commun.* **2020**, *11*, 1180.
- [4] J. Liu, D. Yan, W. Pang, Y. Zhang, *Mater. Today* **2021**, *49*, 324.
- [5] M. Zhu, Z. Yi, B. Yang, C. Lee, *Nano Today* **2021**, *36*, 101016.
- [6] Y. Niu, H. Liu, R. He, Z. Li, H. Ren, B. Gao, H. Guo, G. M. Genin, F. Xu, *Mater. Today* **2020**, *41*, 219.
- [7] H. Yu, N. Li, N. Zhao, *Adv. Energy Mater.* **2021**, *11*, 2002646.
- [8] Y. Gao, C. Xie, Z. Zheng, *Adv. Energy Mater.* **2021**, *11*, 2002838.
- [9] Z. Li, Y. An, S. Dong, C. Chen, L. Wu, Y. Sun, X. Zhang, *Energy Storage Mater.* **2020**, *31*, 252.
- [10] P. Rui, W. Zhang, P. Wang, *ACS Nano* **2021**, *15*, 6949.
- [11] L. Chen, C. Chen, L. Jin, H. Guo, A. C. Wang, F. Ning, Q. Xu, Z. Du, F. Wang, Z. L. Wang, *Energy Environ. Sci.* **2021**, *14*, 955.
- [12] D. W. Jin, Y. J. Ko, C. W. Ahn, S. Hur, T. K. Lee, D. G. Jeong, M. Lee, C.-Y. Kang, J. H. Jung, *Small* **2021**, *17*, 2007289.

- [13] L. Lan, J. Xiong, D. Gao, Y. Li, J. Chen, J. Lv, J. Ping, Y. Ying, P. S. Lee, *ACS Nano* **2021**, *15*, 5307.
- [14] H. Ko, Y. W. Lim, S. Han, C. K. Jeong, S. B. Cho, *ACS Energy Lett.* **2021**, *6*, 2792.
- [15] S. Park, J. Park, Y. G. Kim, S. Bae, T. W. Kim, K. I. Park, B. H. Hong, C. K. Jeong, S. K. Lee, *Nano Energy* **2020**, *78*, 105266.
- [16] H. Askari, A. Khajepour, M. B. Khamesee, Z. Saadatnia, Z. L. Wang, *Nano Today* **2018**, *22*, 10.
- [17] T. Huang, C. Wang, H. Yu, H. Wang, Q. Zhang, M. Zhu, *Nano Energy* **2015**, *14*, 226.
- [18] Y. Guo, X.-S. Zhang, Y. Wang, W. Gong, Q. Zhang, H. Wang, J. Brugger, *Nano Energy* **2018**, *48*, 152.
- [19] J. He, S. Qian, X. Niu, N. Zhang, J. Qian, X. Hou, J. Mu, W. Geng, X. Chou, *Nano Energy* **2019**, *64*, 103933.
- [20] S. Maiti, S. K. Karan, J. K. Kim, B. B. Khatua, *Adv. Energy Mater.* **2019**, *9*, 1803027.
- [21] X. Wang, B. Yang, J. Liu, Y. Zhu, C. Yang, Q. He, *Sci. Rep.* **2016**, *6*, 36409.
- [22] J. Zhu, Y. Zhu, X. Wang, *Adv. Mater. Interfaces* **2018**, *5*, 1700750.
- [23] W.-Z. Song, X.-X. Wang, H.-J. Qiu, N. Wang, M. Yu, Z. Fan, S. Ramakrishna, H. Hu, Y.-Z. Long, *Nano Energy* **2021**, *82*, 105695.
- [24] Z. Qin, Y. Yin, W. Zhang, C. Li, K. Pan, *ACS Appl. Mater. Interfaces* **2019**, *11*, 12452.
- [25] Y. Wu, J. Qu, W. A. Daoud, L. Wang, T. Qi, *J. Mater. Chem. A* **2019**, *7*, 13347.
- [26] S. Badatya, A. Kumar, C. Sharma, A. K. Srivastava, J. P. Chaurasia, M. K. Gupta, *Mater. Lett.* **2021**, *290*, 129493.
- [27] H. Fu, Y. Jin, H. Ou, P. Huang, C. Liu, Y. Luo, Z. Xiao, *J. Mater. Sci.: Mater. Electron.* **2021**, *32*, 21178.
- [28] P. Huang, S. Xu, W. Zhong, H. Fu, Y. Luo, Z. Xiao, M. Zhang, *Sens. Actuator, A* **2021**, *330*, 112880.
- [29] D. Ponnamma, O. Aljarod, H. Parangusan, M. A. Ali Al-Maadeed, *Mater. Chem. Phys.* **2020**, *239*, 122257.
- [30] H. Ren, S. Yu, L. Chao, Y. Xia, Y. Sun, S. Zuo, F. Li, T. Niu, Y. Yang, H. Ju, B. Li, H. Du, X. Gao, J. Zhang, J. Wang, L. Zhang, Y. Chen, W. Huang, *Nat. Photonics* **2020**, *14*, 154.
- [31] S.-F. Leung, K.-T. Ho, P.-K. Kung, V. K. S. Hsiao, H. N. Alshareef, Z. L. Wang, J.-H. He, *Adv. Mater.* **2018**, *30*, 1704611.
- [32] G. Pacchioni, *Nat. Rev. Mater.* **2021**, *6*, 108.
- [33] Y. Wang, J. Duan, X. Yang, L. Liu, L. Zhao, Q. Tang, *Nano Energy* **2020**, *69*, 104418.
- [34] R. Pandey, G. Sb, S. Grover, S. K. Singh, A. Kadam, S. Ogale, U. V. Waghmare, V. R. Rao, D. Kabra, *ACS Energy Lett.* **2019**, *4*, 1004.
- [35] S. M. Shah, A. Kira, H. Imahori, D. Ferry, H. Brisset, F. Fages, J. Ackermann, *J. Colloid Interface Sci.* **2012**, *386*, 268.
- [36] F. Zheng, W.-L. Xu, H.-D. Jin, X.-T. Hao, K. P. Ghiggino, *RSC Adv.* **2015**, *5*, 89515.
- [37] J. Kang, S. Tongay, J. Zhou, J. Li, J. Wu, *Appl. Phys. Lett.* **2013**, *102*, 012111.
- [38] X. Jiang, F. Wang, Q. Wei, H. Li, Y. Shang, W. Zhou, C. Wang, P. Cheng, Q. Chen, L. Chen, Z. Ning, *Nat. Commun.* **2020**, *11*, 1245.
- [39] S. M. Menke, N. A. Ran, G. C. Bazan, R. H. Friend, *Joule* **2018**, *2*, 25.
- [40] M. Chen, M.-G. Ju, A. D. Carl, Y. Zong, R. L. Grimm, J. Gu, X. C. Zeng, Y. Zhou, N. P. Padture, *Joule* **2018**, *2*, 558.
- [41] Y. Chen, H. Zhou, *J. Appl. Phys.* **2020**, *128*, 060903.
- [42] A. Musiienko, J. Pipek, P. Praus, M. Brynza, E. Belas, B. Dryzhakov, M.-H. Du, M. Ahmadi, R. Grill, *Sci. Adv.* **2020**, *6*, eabb6393.
- [43] R. Ding, X. Zhang, G. Chen, H. Wang, R. Kishor, J. Xiao, F. Gao, K. Zeng, X. Chen, X. W. Sun, Y. Zheng, *Nano Energy* **2017**, *37*, 126.
- [44] A. Sultana, M. M. Alam, P. Sadhukhan, U. K. Ghorai, S. Das, T. R. Middy, D. Mandal, *Nano Energy* **2018**, *49*, 380.
- [45] A. Sultana, S. K. Ghosh, M. M. Alam, P. Sadhukhan, K. Roy, M. Xie, C. R. Bowen, S. Sarkar, S. Das, T. R. Middy, D. Mandal, *ACS Appl. Mater. Interfaces* **2019**, *11*, 27279.
- [46] A. Sultana, P. Sadhukhan, M. M. Alam, S. Das, T. R. Middy, D. Mandal, *ACS Appl. Mater. Interfaces* **2018**, *10*, 4121.
- [47] V. Jella, S. Ippili, J.-H. Eom, Y.-J. Kim, H.-J. Kim, S.-G. Yoon, *Nano Energy* **2018**, *52*, 11.
- [48] D. B. Kim, K. H. Park, Y. S. Cho, *Energy Environ. Sci.* **2020**, *13*, 2077.
- [49] S. Ippili, V. Jella, J.-H. Eom, J. Kim, S. Hong, J.-S. Choi, V.-D. Tran, N. Van Hieu, Y.-J. Kim, H.-J. Kim, S.-G. Yoon, *Nano Energy* **2019**, *57*, 911.
- [50] B. Yang, J. Chen, F. Hong, X. Mao, K. Zheng, S. Yang, Y. Li, T. Pullerits, W. Deng, K. Han, *Angew. Chem., Int. Ed.* **2017**, *56*, 12471.
- [51] M. Leng, Y. Yang, K. Zeng, Z. Chen, Z. Tan, S. Li, J. Li, B. Xu, D. Li, M. P. Hautzinger, Y. Fu, T. Zhai, L. Xu, G. Niu, S. Jin, J. Tang, *Adv. Funct. Mater.* **2018**, *28*, 1704446.
- [52] J. Gu, H. Gu, J. Cao, S. Chen, N. Li, J. Xiong, *Appl. Surf. Sci.* **2018**, *439*, 589.
- [53] X. Mao, Y. Chen, Y. Si, Y. Li, H. Wan, J. Yu, G. Sun, B. Ding, *RSC Adv.* **2013**, *3*, 7562.
- [54] X. Gu, N. Li, J. Cao, J. Xiong, *Polym. Eng. Sci.* **2018**, *58*, 1381.
- [55] Y. Li, J. Xiong, J. Lv, J. Chen, D. Gao, X. Zhang, P. S. Lee, *Nano Energy* **2020**, *78*, 105358.
- [56] S. Mondal, T. Paul, S. Maiti, B. K. Das, K. K. Chattopadhyay, *Nano Energy* **2020**, *74*, 104870.
- [57] L. Romani, A. Speltini, C. N. Dibenedetto, A. Listorti, F. Ambrosio, E. Mosconi, A. Simbula, M. Saba, A. Profumo, P. Quadrelli, F. De Angelis, L. Malavasi, *Adv. Funct. Mater.* **2021**, *31*, 2104428.
- [58] L.-C. Chen, Z.-L. Tseng, J.-K. Huang, *Nanomaterials* **2016**, *6*, 183.
- [59] D. Shi, V. Adinolfi, R. Comin, M. Yuan, E. Alarousu, A. Buin, Y. Chen, S. Hoogland, A. Rothenberger, K. Katsiev, Y. Losovyj, X. Zhang, P. A. Dowben, O. F. Mohammed, E. H. Sargent, O. M. Bakr, *Science* **2015**, *347*, 519.
- [60] Q. Dong, Y. Fang, Y. Shao, P. Mulligan, J. Qiu, L. Cao, J. Huang, *Science* **2015**, *347*, 967.
- [61] X.-K. Liu, W. Xu, S. Bai, Y. Jin, J. Wang, R. H. Friend, F. Gao, *Nat. Mater.* **2021**, *20*, 10.
- [62] H. Zou, Y. Zhang, L. Guo, P. Wang, X. He, G. Dai, H. Zheng, C. Chen, A. C. Wang, C. Xu, Z. L. Wang, *Nat. Commun.* **2019**, *10*, 1427.
- [63] K. A. Bogdanowicz, D. Augustowski, J. Dziedzic, P. Kwaśnicki, W. Malej, A. Iwan, *Materials* **2020**, *13*, 2721.
- [64] H. Paik, Y.-Y. Choi, S. Hong, K. No, *Sci. Rep.* **2015**, *5*, 13209.
- [65] J. Lv, G. Thangavel, Y. Li, J. Xiong, D. Gao, J. Ciou, M. W. M. Tan, I. Aziz, S. Chen, J. Chen, X. Zhou, W. C. Poh, P. S. Lee, *Sci. Adv.* **2021**, *7*, eabg8433.
- [66] X. Yang, S. Chan, L. Wang, W. A. Daoud, *Nano Energy* **2018**, *44*, 388.
- [67] J. Du, X. Yang, J. Duan, Y. Wang, Q. Tang, *Nano Energy* **2020**, *70*, 104514.
- [68] J. Du, J. Duan, X. Yang, Y. Wang, Y. Duan, Q. Tang, *Nano Energy* **2020**, *74*, 104845.
- [69] D. Mandal, K. Henkel, D. Schmeißer, *Phys. Chem. Chem. Phys.* **2014**, *16*, 10403.
- [70] J. Xiong, P. Cui, X. Chen, J. Wang, K. Parida, M.-F. Lin, P. S. Lee, *Nat. Commun.* **2018**, *9*, 4280.
- [71] Y. Wang, X. Yang, X. Yu, J. Duan, Q. Yang, Y. Duan, Q. Tang, *Nano Energy* **2020**, *77*, 105280.
- [72] G. Xie, X. Yang, J. Duan, Y. Duan, Q. Tang, *J. Mater. Chem. A* **2020**, *8*, 11966.
- [73] D. B. Kim, K. S. Park, S. J. Park, Y. S. Cho, *Nano Energy* **2022**, *92*, 106785.
- [74] A. A. Khan, G. Huang, M. M. Rana, N. Mei, M. Biondi, S. Rassel, N. Tanguy, B. Sun, Z. Leonenko, N. Yan, C. Wang, S. Xu, D. Ban, *Nano Energy* **2021**, *86*, 106039.
- [75] J. Shen, Z. Li, J. Yu, B. Ding, *Nano Energy* **2017**, *40*, 282.
- [76] D. Jang, Y. Kim, T. Y. Kim, K. Koh, U. Jeong, J. Cho, *Nano Energy* **2016**, *20*, 283.